






## Article

# Compositional Design and Thermal Processing of a Novel Lead-Free Cu–Zn–Al–Sn Medium Entropy Brass Alloy

Spyridon Chaskis <sup>1,\*</sup>, Stavroula Maritsa <sup>1</sup>, Paul Stavroulakis <sup>2</sup>, Sofia Papadopoulou <sup>3</sup>, Russell Goodall <sup>2</sup> and Spyros Papaefthymiou <sup>1</sup>

<sup>1</sup> Laboratory of Physical Metallurgy, Division of Metallurgy and Materials, School of Mining and Metallurgical Engineering, National Technical University of Athens, 9, Heroon Polytechniou Street, 15780 Athens, Greece; maritsastavroula@mail.ntua.gr (S.M.); spapaef@metal.ntua.gr (S.P.)

<sup>2</sup> Department of Materials Science & Engineering, The University of Sheffield, Sir Robert Hadfield Building, Portobello Str., Sheffield S1 3JD, UK; ppstavroulakis1@sheffield.ac.uk or pstavntua@gmail.com (P.S.); r.goodall@sheffield.ac.uk (R.G.)

<sup>3</sup> Department of Physical Metallurgy and Forming, Hellenic Research Centre for Metals (ELKEME S.A.), 61st km Athens-Lamia National Road, 32011 Oinofyta, Greece; spapadopoulou@elkeme.gr

\* Correspondence: schaskis@metal.ntua.gr or xspiros97@hotmail.com

**Abstract:** In the current work, a novel medium entropy copper alloy was designed with the aim of avoiding the use of expensive, hazardous or scarce alloying elements and instead employing widely available and cost-effective alternatives. In order to investigate this unknown region of multicomponent alloy compositions, the thermo-physical parameters were calculated and the CALPHAD method was utilized. This led to the design of the Cu<sub>50</sub>Zn<sub>25</sub>Al<sub>20</sub>Sn<sub>5</sub> at. % (Cu<sub>53.45</sub>Zn<sub>27.49</sub>Al<sub>9.08</sub>Sn<sub>9.98</sub> wt. %) alloy with a relatively low density of 6.86 g/cm<sup>3</sup> compared with conventional brasses. The designed alloy was manufactured through vacuum induction melting, producing two ingots weighing 1.2 kg each, which were subjected to a series of heat treatments. The microstructural evolution of the alloy in the as-cast and heat-treated conditions was assessed through optical and scanning electron microscopy. The hardness of the as-cast and heat-treated alloy at room temperature was also studied. The alloy was characterized by a multiphase microstructure containing a major Cu-rich (Cu–Zn–Al) matrix reinforced with a secondary Zn-rich (Zn–Cu) phase and pure Sn. In terms of mechanical properties, the developed alloy exhibited high hardness values of roughly 378 HV<sub>0.2</sub> and 499 HV<sub>0.2</sub> in the as-cast and heat-treated conditions, respectively.

**Keywords:** copper-based alloys; medium-entropy alloys; casting; lightweight alloys; CALPHAD; microstructure; mechanical properties; heat treatment



**Citation:** Chaskis, S.; Maritsa, S.; Stavroulakis, P.; Papadopoulou, S.; Goodall, R.; Papaefthymiou, S. Compositional Design and Thermal Processing of a Novel Lead-Free Cu–Zn–Al–Sn Medium Entropy Brass Alloy. *Metals* **2024**, *14*, 620. <https://doi.org/10.3390/met14060620>

Academic Editor: Jiro Kitagawa

Received: 28 April 2024

Revised: 20 May 2024

Accepted: 21 May 2024

Published: 24 May 2024



**Copyright:** © 2024 by the authors. Licensee MDPI, Basel, Switzerland. This article is an open access article distributed under the terms and conditions of the Creative Commons Attribution (CC BY) license (<https://creativecommons.org/licenses/by/4.0/>).

## 1. Introduction

Copper-zinc (Cu–Zn) alloys, broadly known as brasses, are considered one of the more important Cu-based alloys. They are used in a wide range of industries due to their good combination of chemical, mechanical and physical properties, while maintaining a low production and manufacturing cost, owing particularly to their impressive machinability [1–4]. The form of chips is perhaps the most crucial factor to consider when evaluating machinability. Discontinuous chip formation favors the efficient disposal of machined material [3,5], contributes to an enhanced surface finish, minimizes tool wear and allows for higher cutting speeds [6]. In brasses, the most widespread practice for the optimization of machinability has been the incorporation of lead (Pb), which promotes fine and discontinuous chip formation during machining. Insoluble in Cu, Pb forms distinct, incoherent particles generally termed as “islands”. These act as stress concentration points during the machining process, promoting free-flowing chips and providing lubrication to the cutting tool as Pb is a soft, low-melting-point element, without affecting the mechanical properties

of the brass [3,7]. Nevertheless, the negative effects of Pb on human health and the environment have led to changes in legislation regarding the permissible Pb levels in various applications where brass alloys are required [3,4,6,8,9]. Therefore, there is an imperative need to design alternative Cu-based alloys without the addition of harmful elements like Pb without compromising their properties. Various alternatives to Pb have been proposed, such as additions of Al [10], Sn [11], Si [10,12,13], Bi [14], graphite and Ti, [15,16] with the intention of forming either insoluble elemental phases or appropriate secondary phase particles (SPPs) emulating the effects of Pb in the microstructure. Also, many patents have been claimed, a few recent ones being EP2761042B1 (Mn–Si–Ca additions) [17], CN113106289B (Sn–Si–Al–Ni–Fe additions, Pb < 0.01 wt. %) [18], WO2022103363A2 (Sn–S–Mo–Al–Si additions) [19] and US2022136085A1 (Fe–Mn–Ni–Al–Si–Sn–P additions, Pb < 0.1 wt. %) [20]. Apart from novel alloy design routes, other solutions may include novel heat treatment pathways for conventional Pb-free brasses to enhance their machinability [21] or utilizing alternative materials for the cutting tools [9,22]. All these options, as discussed in the above references, exhibit certain limitations and may result in significant increases in production costs. We believe that addressing these challenges could be achieved by applying the high-entropy alloy (HEA) design concept to these otherwise conventional alloys, resulting in the creation of novel high-entropy brasses (HEBs).

In HEAs, four or more alloying elements are added in percentages between 5 and 35 at. % [23–25]. This allows for greater chemical flexibility, resulting in alloys with properties tailored to specific applications. These include enhanced mechanical properties, corrosion resistance and improved thermodynamic stability [23–25]. Sustainable HEA design has also been at the forefront of the latest developments, especially in the low-density Al-based alloy region, producing low-cost, recyclable alloys with wide raw material availability [26,27]. Although not explicitly stated as such, there have been previous reports of alloys in the literature that could be considered medium-entropy brasses (MEBs) or HEBs. These may include elements such as aluminum (Al), copper (Cu), manganese (Mn), nickel (Ni) and tin (Sn) [24]. Laws et al. [28] presented extensive research on HEBs, where alloys based on the Cu–Mn–Ni ternary system with the addition of Al, Sn and Zn were designed and studied. These alloys were  $[\text{CuMnNi}]_{100-x}\text{Al}_x$  ( $x = 5, 10, 20, 25, 30, 40$ ),  $[\text{CuMnNi}]_{100-x}\text{Sn}_x$  ( $x = 5, 10, 20, 25$ ),  $[\text{CuMnNi}]_{100-x}\text{Zn}_x$  ( $x = 20, 25, 35, 40$ ) and  $[\text{CuMnNi}]_{100-x-y-z}\text{Al}_x\text{Sn}_y\text{Zn}_z$  ( $x = 5, 10, y = 5, 10, z = 10, 20, 35$  at. %). These novel compositions displayed an improvement in strength, hardness and ductility compared with other conventional brass alloys. Nagase et al. [29] designed the HEBs  $\text{CuZnMnNiSn}_{0.2}$  and  $\text{Cu}_2\text{ZnMnNiSn}_{0.4}$  and medium-entropy brasses (MEBs)  $\text{Cu}_x\text{ZnMnNi}$  ( $x = 1, 2, 3, 4$  at. %), where the  $\text{Cu}_x\text{ZnMnNi}$  ( $x = 1, 2$ ) MEBs showed improved ductility, while the Sn addition increased the hardness and reduced the ductility. Nonetheless, the number of reports to date on HEBs and MEBs is limited. However, the rapid development in the field of multicomponent and high-entropy alloys could provide an appealing alternative to the Pb issue encountered in commercial brass alloys.

The main objective of this research was to combine the concept of HEAs with conventional brass alloy design principles to develop a novel grade of Pb-free MEB. These considerations led to the initial selection of the AlCuZnSn system, utilizing alloying elements that are commonly used as base components in brass and bronze alloys. This system was explored using ThermoCalc with the SSOL4: SGTE Alloy Solutions Database v.4.9 database, seeking compositions that would obtain a major solid-solution (SS) phase reinforced with SPPs or insoluble elemental particles, as this would allow additional strengthening, and also the possibility of controlling chip formation on machining. Following this exploration, the composition  $\text{Cu}_{50}\text{Zn}_{25}\text{Al}_{20}\text{Sn}_5$  (at. %) was selected, manufactured through vacuum induction melting (VIM), heat-treated using a range of cooling rates, and characterized in both the as-cast and heat-treated conditions. The developed alloy could offer a lightweight alternative to some other brasses and is compared against the cast C83300-C86XXX Cu-alloys [30], since it was designed combining the elements making up the alloys under those designations.

## 2. Materials and Methods

### 2.1. Computational Methods

In this study, the artificial neural network (ANN) software pyMPEALab Toolkit was utilized for the computation of the thermophysical parameters of the chosen alloy [31]. The software uses empirical parameters to predict phase formation based on the Hume–Rothery rules and additional thermodynamic criteria [32–34]. These consist of the enthalpy of mixing in the liquid phase ( $\Delta H_{\text{mix}}$ ), atomic size difference ( $r$ ), Pauling electronegativity difference ( $\Delta\chi$ ) and the  $\Omega$  parameter. These standalone parameters are not sufficient conditions to accurately predict single-phase solid-solution phase formation [35]. They could, however, be useful as preliminary design indicators to define the likelihood of solid-solution formation in an alloy, and to assist with screening compositions. The Thermocalc<sup>®</sup> software (Version 2022a, Thermo-Calc Software AB, Stockholm, Sweden) with the SSOL4: SGTE Alloy Solutions Database v.4.9 was used to perform CALPHAD predictions [36]. The chosen alloying elements were copper (Cu), aluminum (Al), zinc (Zn) and tin (Sn). The MEB design was based on Cu–Zn alloys, while Al was selected as a cost-effective lightweight addition, as the Cu–Zn–Al system has showed great stability [37–39]. Sn is also a common alloying element in brass alloys [11,40], which CALPHAD indicated could act as an insoluble elemental phase in the present system. The final composition chosen was  $\text{Cu}_{50}\text{Zn}_{25}\text{Al}_{20}\text{Sn}_5$  at. %.

### 2.2. Experimental Methods

The  $\text{Cu}_{50}\text{Zn}_{25}\text{Al}_{20}\text{Sn}_5$  alloy was cast in a vacuum induction melting furnace (“vacuum induction melting—VIM”), using an Arcast-SC100 (Oxford, ME, USA) under a high purity argon atmosphere. The purity of the raw materials used was 99.99 wt. % for Al, Cu and Sn and 99.9 wt. % for Zn. Two  $125 \times 50 \times 40$  mm ingots were cast (designated as C1, C2) weighing 1200 g each. The casting temperature of the ingots was 990 °C for C1 and 960 °C for ingot C2. The microstructure of the as-cast and heat-treated conditions was studied to evaluate the suitability and behavior of the developed MEA. Ingot C1 was sectioned longitudinally, and two samples were studied (Figure 1a). Sample A1 was subjected to macroetching to study the macrostructure and solidification zones of the cast, and sample A2 was sectioned into multiple samples to study the microstructure and segregation phenomena (Figure 1b). In addition, a transverse section near the middle of ingot C2 was made (Figure 1c). Two samples were studied; sample B1 was macroetched and sample B2 was sectioned into multiple samples (Figure 1, Table 1).

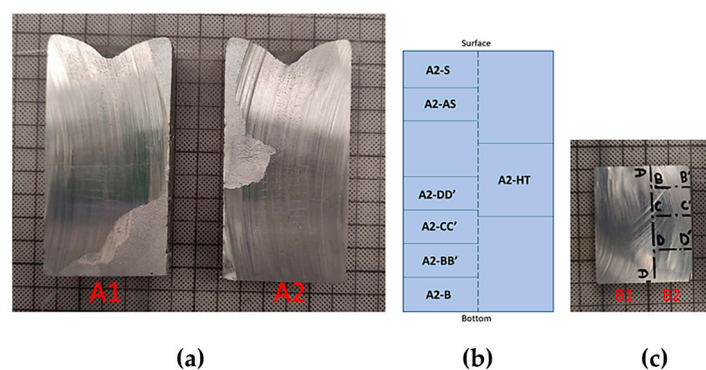


**Figure 1.** (a) Samples A1 and A2 originating from ingot C1. (b) Multiple sections of sample A2. (c) Samples B1 and B2 originating from ingot C2.

**Table 1.** Designation for the studied specimens.

Samples	Description
A2-S, A2-AS, A2-BB', A2-CC', A2-DD', A2-B	As-cast samples, sections from sample A2.
B2-BB', B2-CC', B2-DD', B2-EE'	As-cast samples, sections from sample B2.
A1, B1	Samples for the study of solidification zones.
T16AC, T16WQ, T16FC	Samples for heat treatment.

Samples were extracted from the area A2-HT, as shown in Figure 1b, and were subjected to heat treatment. The same area of extraction was used to ensure the comparison of regions with similar chemical composition and avoid the effect of potential segregation phenomena. The heat treatments were carried out at 550 °C for a duration of 16 h, followed by furnace cooling (FC), air cooling (AC) or water quenching (WQ). Through this we aimed at investigating the phase stability and formation process as a function of the cooling rate from a specific temperature. To achieve this, 3 different heat treatments were performed at 550 °C utilizing different cooling rates, which are presented in Table 2.

**Table 2.** Scheme of homogenizations conducted at 550 °C (FC—furnace cooling, AC—air cooling, WQ—water quench).

Sample	Time (Hours)	Cooling Method
T16AC	16	AC
T16WQ	16	WQ
T16FC	16	FC

Metallographic preparation was carried out according to standard metallographic procedures. The samples were cold mounted in resin, ground with 80, 220, 500 and 1200 grit papers, and polished using diamond suspensions of 3 µm (Struers DiaPro Mol B3, Copenhagen, Denmark), 1 µm (Struers DiaPro Nap B1) and 0.04 µm colloidal silica (Struers OP-U NonDry) in succession. Samples A1 and B1 were macroetched to reveal the solidification zones. As such, a series of etching reagents (RI-RIV) were trialed to reveal the macrostructure of the cast samples (Table 3). Among those, RIII was proven to be the most effective.

**Table 3.** Compositions and etching duration of the macroetchants tested.

Etchant	RI (Tucker's Etch)	RII (Diluted HNO <sub>3</sub> )	RIII (HNO <sub>3</sub> )	RIV (FeCl <sub>3</sub> )
Composition	25 mL H <sub>2</sub> O 15 mL HNO <sub>3</sub> 45 mL HCl 15 mL HF	10 mL HNO <sub>3</sub> 90 mL H <sub>2</sub> O	50 mL HNO <sub>3</sub> 50 mL H <sub>2</sub> O	30 mL HCl 10 g FeCl <sub>3</sub> 120 mL H <sub>2</sub> O
Etching Duration (s)	300	300	30	60

The study of the macrostructure and solidification zones was carried out using a Nikon SMZ 1500 stereoscope (Nikon, Tokyo, Japan). For the evaluation of the microstructure and chemical composition of various regions, an Epiphot 300 (Nikon, Tokyo, Japan) optical microscope and a JEOL JSM-IT800 scanning electron microscope (SEM, Tokyo, Japan), equipped with energy-dispersive X-ray spectrometry (EDS) for high-resolution images and elemental analysis data acquisition, were used. Six specimens (as-cast A2-S, A2-DD' & A2-B, heat-treated T16AC, T16WQ, T16FC) were chosen for analysis through means of electron microscopy. The three as-cast specimens were chosen in order to evaluate compositional variations along the height of cast A, while the 16 h heat-treated are representative of all the microstructures that can be obtained for each cooling rate.



A Vickers hardness Duramin-40 M1 model (Struers, Copenhagen, Denmark) measurer was employed on the polished sample surface using a 0.2 kg load, applied for 10 s. At least 10 random individual measurements were made for each test.

### 3. Results and Discussion

#### 3.1. Thermo-Physical Parameters for Phase Formation in HEAs

The thermo-physical parameters concerning theoretical phase formation in the  $\text{Cu}_{50}\text{Zn}_{25}\text{Al}_{20}\text{Sn}_5$  alloy are presented in Table 4. These can provide an estimate of the likelihood of solid-solution phase formation and are intended to be used as empirical indicators, not a definitive guide. It is important to consider that it is generally very difficult to keep the  $\Delta H_{\text{mix}}$  values within the limits for solid-solution (SS) phase formation [41]. The theoretical density of the alloy was calculated using the rule of mixtures.

**Table 4.** Thermo-physical parameters and the theoretical density for the developed alloy.

$\Delta H_{\text{mix}}$ (kJ/mol)	$\delta$ (%)	$\Delta S_{\text{mix}}$ (J/K/mol)	$\Omega$	$\Delta\chi$	VEC	$T_m$ (K)
0.1	6.62	9.68	105.93	0.14	9.3	1063.89

The  $\Delta H_{\text{mix}}$  of this system lies within the range of  $-1$  to  $5$  kJ/mole that is required for the formation of SS [41]. Complementary criteria concerning the formation of SS in alloys containing low-density elements are  $\delta$  values below  $4.5\%$ ,  $\Delta\chi$  equal or below  $0.175$  and  $\Omega$  higher than  $1.1$  [41]. In this case, only the  $\delta$  criterion is not satisfied. Therefore, a microstructure predominantly characterized by a face-centered cubic (FCC) phase would be expected to be stabilized at room temperature under equilibrium conditions.

#### 3.2. CALPHAD Methodology and Equilibrium Phase Diagram

The calculated pseudo binary phase diagram of the AlCuZnSn system as a function of the Sn addition using ThermoCalc with the SSOL4: SGTE Alloy Solutions Database v.4.9 is depicted in Figure 2. It provides information for possible phases that can be formed in the alloy and is a useful tool for screening out chemical compositions and aids in the alloy development process. After an extensive investigation, the phase diagram was calculated for the composition  $\text{Cu}_{50}\text{Zn}_{25}\text{Al}_{20}\text{Sn}_5$  at. %. According to the calculations, the alloy should be characterized by a single high-temperature BCC phase between  $460$  and  $810$  °C, thus deeming it heat treatable. The formation of secondary phase particles (SPPs) at lower temperatures could have a positive effect on the alloy's strength and machinability, respectively, based on the literature concerned [6]. Furthermore, the formation of insoluble elemental Sn particles was observed. These could behave similarly to Pb, acting as crack-concentration points and providing tool lubrication, thus having a positive effect on the machinability of the alloy [3,42].

The liquidus was predicted at  $910$  °C, while the solidus at  $810$  °C pointed at a solidification range of roughly  $100$  °C. The first solvus line is encountered at  $460$  °C, where  $\delta$ -AlCu is formed, thus progressively depleting the BCC solid solution of Cu and Al. A second solvus line is encountered at  $250$  °C, where the formation of  $\gamma$ -CuZn takes place through the further decomposition of the BCC solid solution. However, it is unclear which temperature variant corresponds to the  $\gamma$ -phase, that being  $\gamma$  or  $\gamma'$ . A third solvus line is encountered at  $147$  °C, where the partial transformation of  $\delta$ -AlCu to  $\gamma$ -AlCu occurs. At room temperature, the BCC matrix phase has fully decomposed, resulting in the formation of insoluble Sn, while the  $\delta \rightarrow \gamma$ -AlCu phase transformation is completed. The designed alloy should thus be composed from a mixture of four different phases at the equilibrium state: a BCC solid solution, the  $\gamma$ -AlCu and  $\gamma$ -CuZn intermetallic phases (IM), and pure Sn.

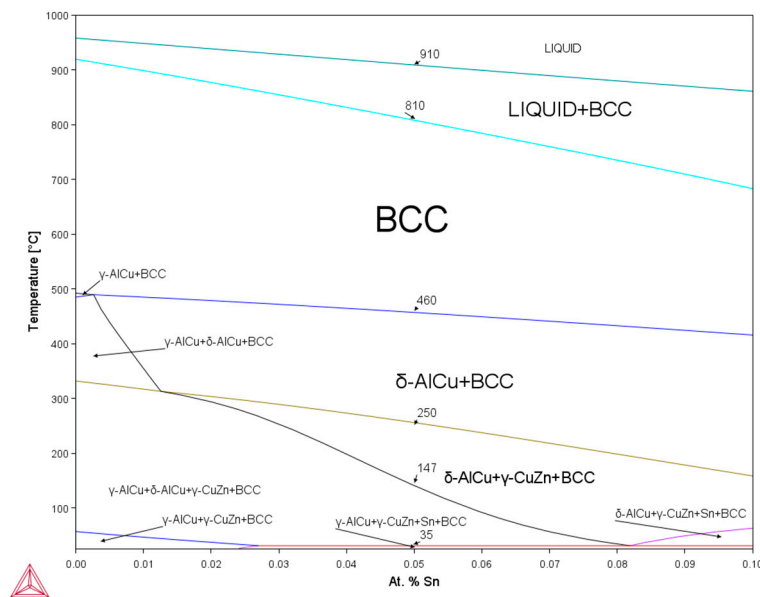


**Figure 2.** Calculated phase diagram of the  $\text{Cu}_{50}\text{Zn}_{25}\text{Al}_{20}\text{Sn}_5$  at. % system with Thermo-Calc Software using the SSOL4: SGTE Alloy Solutions database.

According to the calculated mole fraction diagram depicted in Figure 3, the mole fraction of the BCC phase is progressively reduced in favor of the formation of the IMs and eventually Sn. The rate of decomposition is accelerated near the initial stages of IM formation at 460 °C and 250 °C but seems unaffected by the formation of the  $\gamma$ -AlCu phase at 147 °C. Instead, the  $\delta \rightarrow \gamma$ -AlCu phase transformation results in the complete absence of  $\delta$ -AlCu at 35 °C. A summary of the phases present in regions of interest concerning the investigated composition is presented in Table 5. The CALPHAD calculations seem to contradict the predictions originally made in Section 3.1, where the expected phase structure was considered to comprise predominantly an FCC solid solution. Both predictions could make sense from a literature standpoint. A 2:1 ratio of Cu:Zn is known to produce  $\alpha$ -brass (FCC), while the progressive depletion of the matrix phase towards the formation of IMs could lead to that ratio shifting in favor of the formation of  $\beta$ -brass (BCC) [6,12,43]. It is also known that alloying elements such as Si or in this case Al operate as  $\beta$  stabilizers, while larger amounts of Al have led to the formation of dual-phase  $\beta$ + $\gamma$ -brass microstructures. The latter case is further supported by the CALPHAD calculations. Nevertheless, our calculations also indicated that the BCC matrix phase is nearly entirely depleted at room temperature (RT), while the microstructure is instead intermetallic (IM) dominated. However, it is not certain that all phase transformations present in the CALPHAD approach will take place, as ThermoCalc calculations are known to overestimate the tendency of Al to form IMs in multicomponent systems [44]. Regardless, both tools were used to provide an insight in aiding the computational design of the alloy, likely leading to the formation of a BCC matrix phase, alongside IMs and potentially elemental Sn.

**Table 5.** Crystallographic properties and compositions of phases evident in the  $\text{Cu}_{50}\text{Zn}_{25}\text{Al}_{20}\text{Sn}_5$  alloy at equilibrium and paraequilibrium states according to CALPHAD.

Phases	Chemical Composition (Mole Percent)	Pearson Notation	Temp. Range	Symmetry/Space Group
BCC	Varied	cI2	RT-910 °C	$\text{Im } \bar{3} \text{ m}$
$\gamma$ -AlCu	$\text{Al}_{0.37}\text{Cu}_{0.63}$	cI52/cP52	RT-147 °C	$\bar{1}43 \text{ m}/\text{P}43 \text{ m}$
$\delta$ -AlCu	$\text{Al}_{0.4}\text{Cu}_{0.6}$	hR52	35-460 °C	R3 m
$\gamma$ -CuZn	$\text{Cu}_{0.35}\text{Zn}_{0.65}$	cI52	RT-250 °C	$\bar{1}43 \text{ m}$
Sn	Pure Sn	tI4/cF8	RT-35 °C	$\bar{1}4 \text{ mm}/\text{Fd}3 \text{ m}$

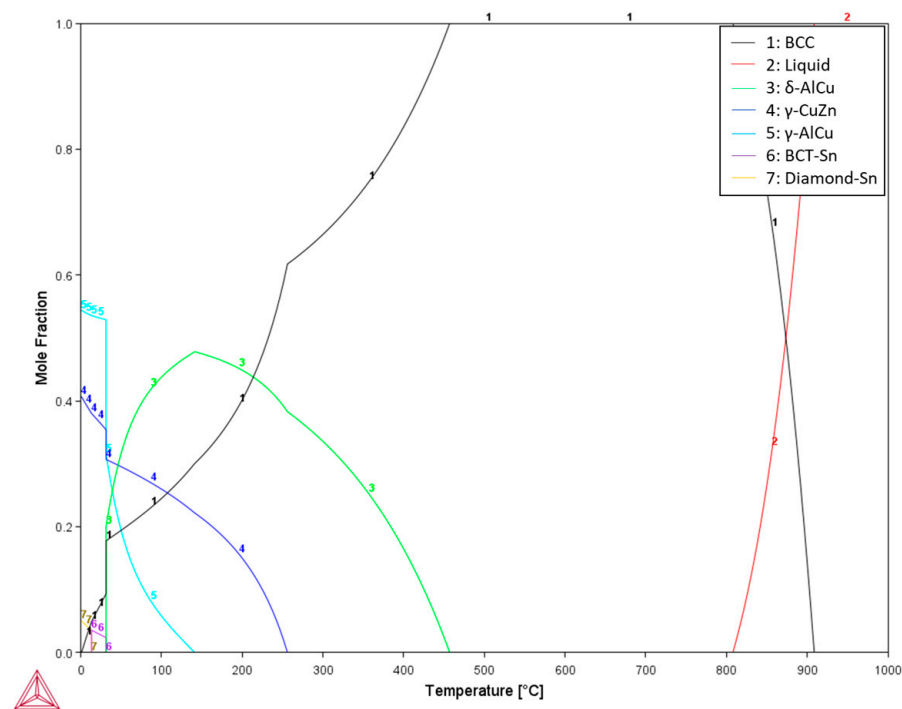


**Figure 3.** Calculated mole fraction diagram of the Cu50Zn25Al20Sn5 at. % system with Thermo-Calc Software using the SSOL4: SGTE Alloy Solutions database.

### 3.3. Solidification Zones

For the macroetching process, the concentrated  $\text{HNO}_3$  etchant RIII (50 mL  $\text{HNO}_3$ , 50 mL  $\text{H}_2\text{O}$ ) showed optimal etching results compared with the other reagents. Etchants RI (Tucker's etch), RII (diluted  $\text{HNO}_3$ ) and RIV ( $\text{FeCl}_3$ ), which are used for aluminum and its alloys, did not have an even effect along the various surface regions of sample A1. RI and RIV managed to unveil the macrostructure exclusively in the upper central region of the ingot, which was closer to the surface. RII instead, mainly used in Cu alloys, showed superior etching results towards the lower part of the ingot. Sample B1 was etched uniformly by all four etchants mentioned above. After successful macroetching (sample A1—Figure 4), it became obvious that the columnar zone was completely absent from the cast, which could be attributed to the high solidification rate. Instead, the cast consisted entirely of equiaxed grains, while in some regions at the mold–cast interface the existence of the freezing zone was observed. This occurred mainly in the upper part of the cast where the grains were coarser. Regarding the equiaxed zone, it was expected that the grain size would vary depending on the distance between the area of interest and the casting mold. Near the bottom of the cast, where the melt first met the mold, the solidification rate was the highest and the grain size the smallest compared with the center and surface regions. Therefore, the further away an area of the cast would be from the cast–mold interface, the larger the grain size would be. The presence of porosity in the upper central part of the cast was also notable and expected predominantly due to shrinkage occurring during the solidification process; this feature does not otherwise influence the outcome of the present study and is easily addressed on an industrial scale. From the perspective of the macrostructure, no significant macrosegregation phenomena were observed.



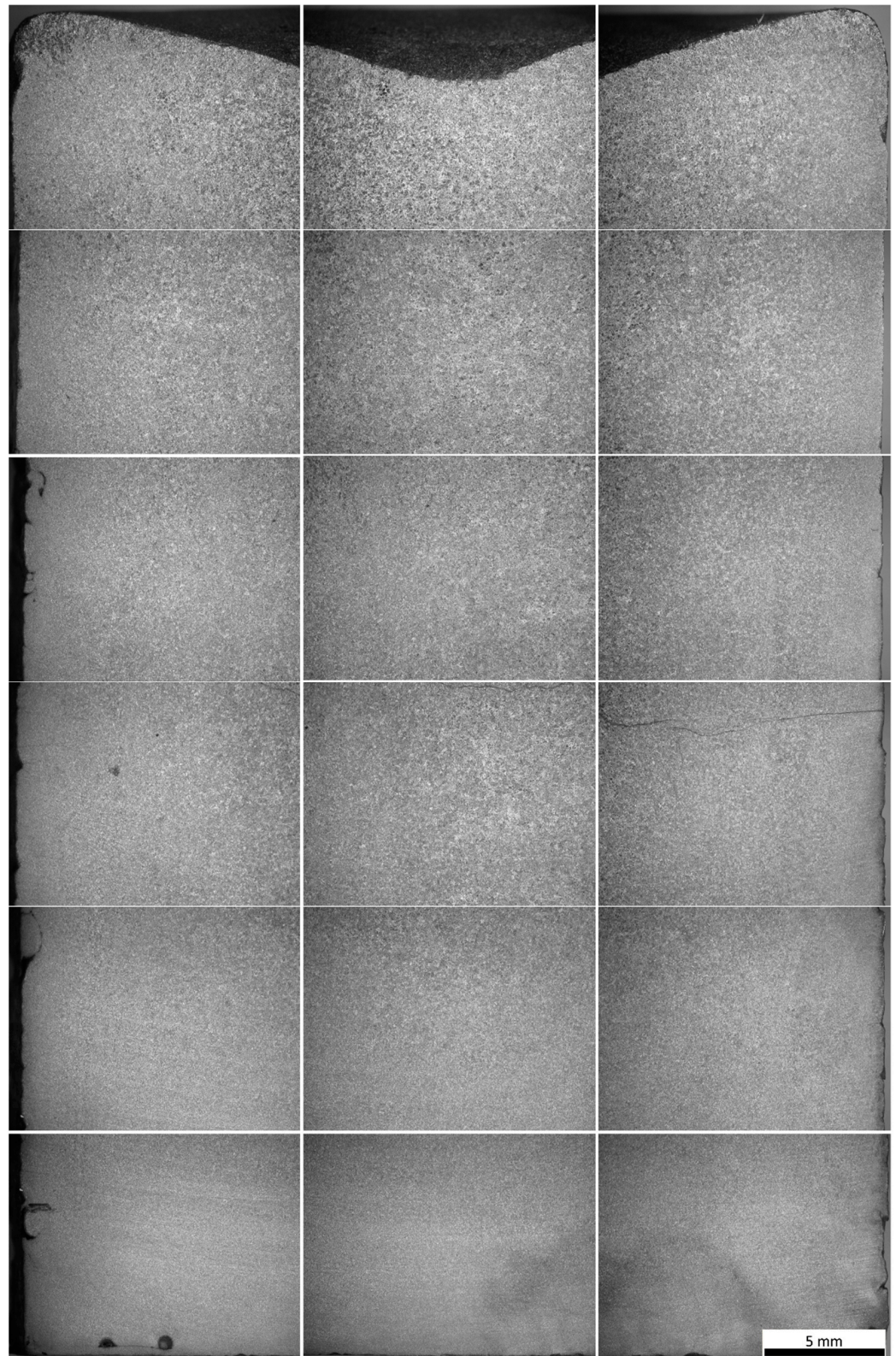


**Figure 4.** Surface of sample A1 after macroetching with RIII etchant (concentrated  $\text{HNO}_3$ ).

### 3.4. Microstructural Characterization

#### 3.4.1. Optical Microscopy

As shown in Figure 5, the as-cast samples were characterized by the existence of predominantly three phases. The darker grey phase occupied the largest volume and was

designated as the primary phase,  $\alpha$ . In addition, a light-colored phase,  $\beta$ , was located at the grain boundaries of phase  $\alpha$  and occupied a smaller volume fraction. The third phase,  $\gamma$ , was also observed around the grains of phase  $\alpha$ . Furthermore, another phase in the form of dark particles was observed along the interphase boundaries of phases  $\alpha$  and  $\gamma$  and were evenly distributed in all as-cast samples. In addition, the samples extracted from the upper part of the ingot showed a greater degree of porosity and coarser grain size, compared with samples from the lower sections. As mentioned before, this was due to the rapid cooling rate near the contact of the material with the mold, resulting in reduced grain size at the lower part of the cast. Furthermore, the presence of porosity near the surface was more pronounced due to gravity forcing trapped air to migrate towards the surface in the melt state through interphase and grain boundaries, and due to shrinkage.

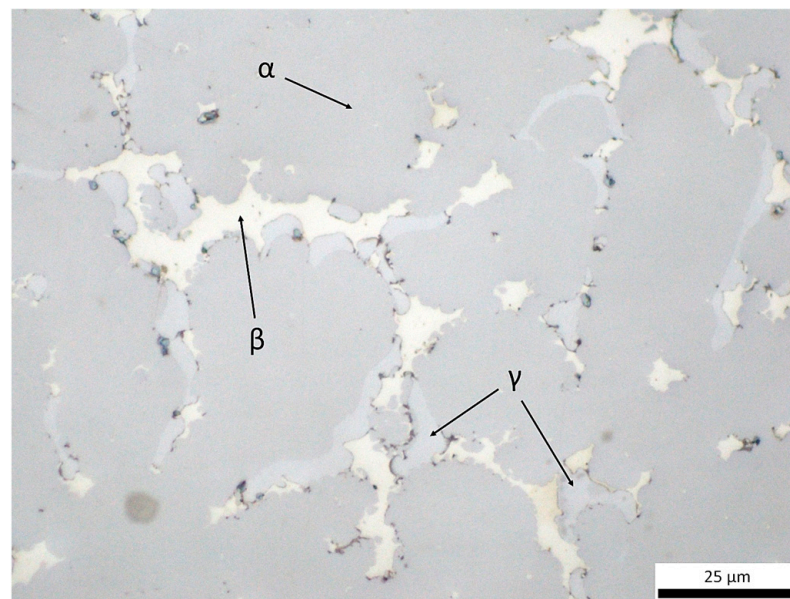


**Figure 5.** Observed phases in sample A2-CC' from the center of the ingot.

Figure 6 shows the microstructure of samples T16WQ, T16AC and T16FC, which were heat treated for 16 h at 550 °C and subsequently water quenched, air cooled and furnace cooled, respectively. In all three samples, two primary phases,  $\alpha'$  (grey colored) and  $\beta'$  (white colored), were evenly distributed, where  $\alpha'$  occupied the larger volume fraction. In the WQ sample T16WQ (Figure 6a,b), the presence of dark particles of small size uniformly distributed in phase  $\beta'$  was observed. In the AC sample T16AC (Figure 6c,d), the presence of scattered particles of two types was noted. These dark-colored particles formed a needle-like or a coarser shape within the volume of phase  $\beta'$ . In addition, the formation of relatively fine  $\gamma'$  (light-grey-colored phase) at the phase  $\alpha'$  grain boundaries was observed. It must be underlined that there was a complete lack of  $\gamma'$  in the WQ condition. In the FC sample T16FC (Figure 6e,f), phases  $\alpha'$  and  $\beta'$  were distributed uniformly, while  $\gamma'$  (light-grey-colored phase) was present with a larger volume fraction compared with the air-cooled sample. This indicates that phase  $\gamma'$  is likely to form at lower temperatures. No particles were observed within phase  $\beta'$ . Instead, small spherical particles had formed at the grain boundaries of phase  $\alpha'$ . As such, the cooling rate seemed to be the definitive factor regarding the microstructural features of the alloy.



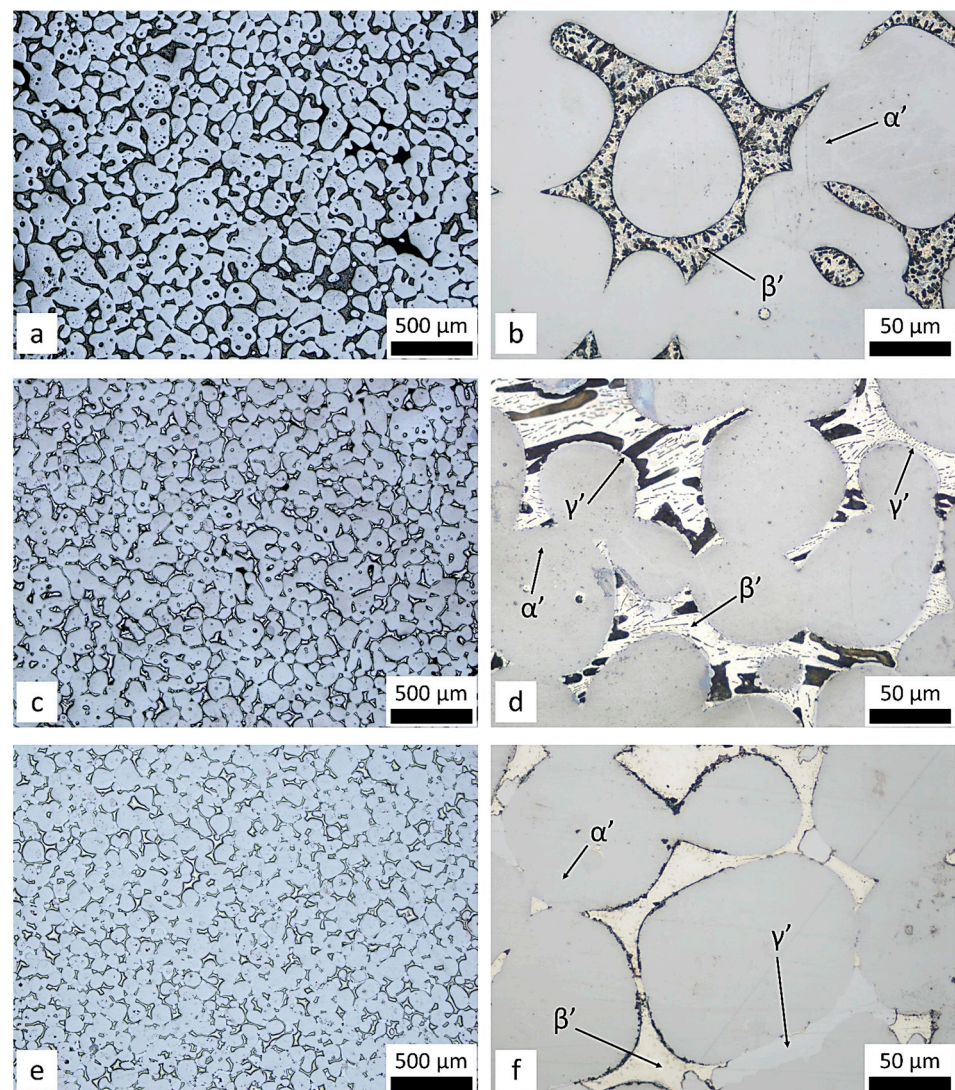


**Figure 6.** Optical microscope images of homogenized samples for 16 h: ((a,b) water-quenched samples, (c,d) air-cooled samples, (e,f) furnace-cooled samples).

### 3.4.2. SEM and EDS Analysis

The overall composition of the alloy estimated using EDS over large areas is presented in Table 6. We note that, even applied over large areas, this technique still provides a relatively localized measure of the composition, rather than taking the ingot as a whole into account. For this analysis, samples from the surface (A2-S), center (A2-DD') and bottom (A2-B) of sample A were studied. It became evident that the deviation from the nominal composition was significant, and therefore the cast suffers from macrosegregation phenomena that could be attributed to the large difference in density between the alloying elements. This issue could be addressed by inducing intensive stirring in the melt or through subsequent thermomechanical processing.

**Table 6.** Elemental composition of the manufactured alloy in as-cast samples A2-S (surface of the cast), A2-DD' (center) and A2-B (bottom) obtained by EDS.

Alloying Elements (at. %)	Cu	Al	Zn	Sn
Nominal	50	20	25	5
Surface	51.97	18.64	27.66	1.73
Center	48.43	20.13	26.35	5.08
Bottom	54.67	9.16	30.85	5.32

Since the microstructure is similar across all of ingot A's geometry, an indicative SEM micrograph of the as-cast state extracted from sample A2-DD' is shown in Figure 7. Analysis at Area 1 revealed that  $\alpha$  is a Cu–Zn–Al SS primary phase, Spot 2 indicated that  $\beta$  is a Sn phase and Spot 1 showed that  $\gamma$  is a Zn-rich Zn–Cu–Al phase (Figure 7). The dark spherical particles that form around the grains of phase  $\alpha$  (Spot 3) exhibited a low amount of O (Table 7). Figure 8 shows the element quant maps for the sample.

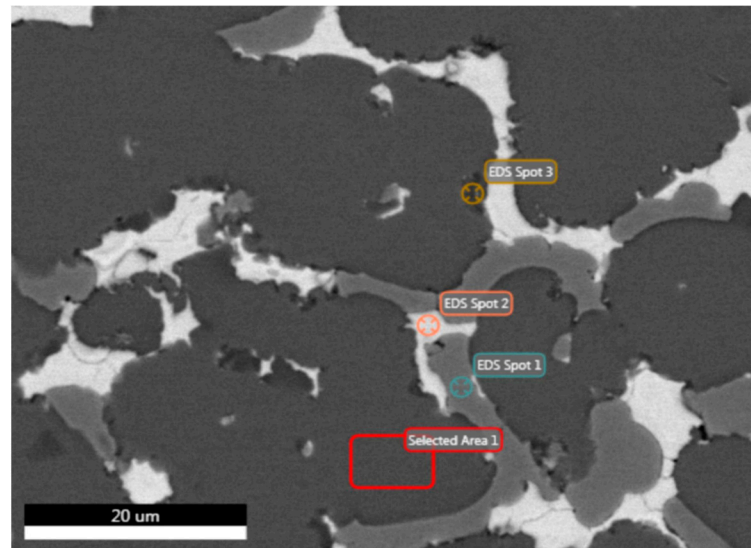


Figure 7. FESEM backscatter electron microstructure with EDS on selected phases for sample A2-DD'.

Table 7. Elemental composition of the manufactured alloy in sample A2-DD' obtained by EDS.

Analysis/ Elements	Spot 1 (at. %)	Spot 2 (at. %)	Spot 3 (at. %)	Area 1 (at. %)
O	0.27	1.15	0.57	0.79
Cu	24.63	9.17	49.80	53.97
Al	2.52	1.34	29.85	20.84
Zn	72.24	7.17	17.39	24.17
Sn	0.33	81.17	2.38	0.24

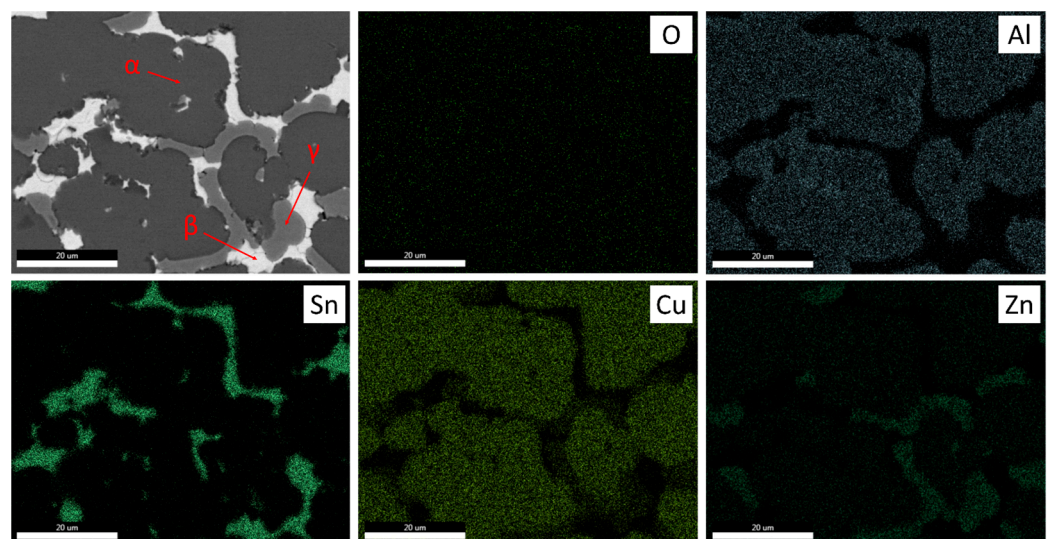
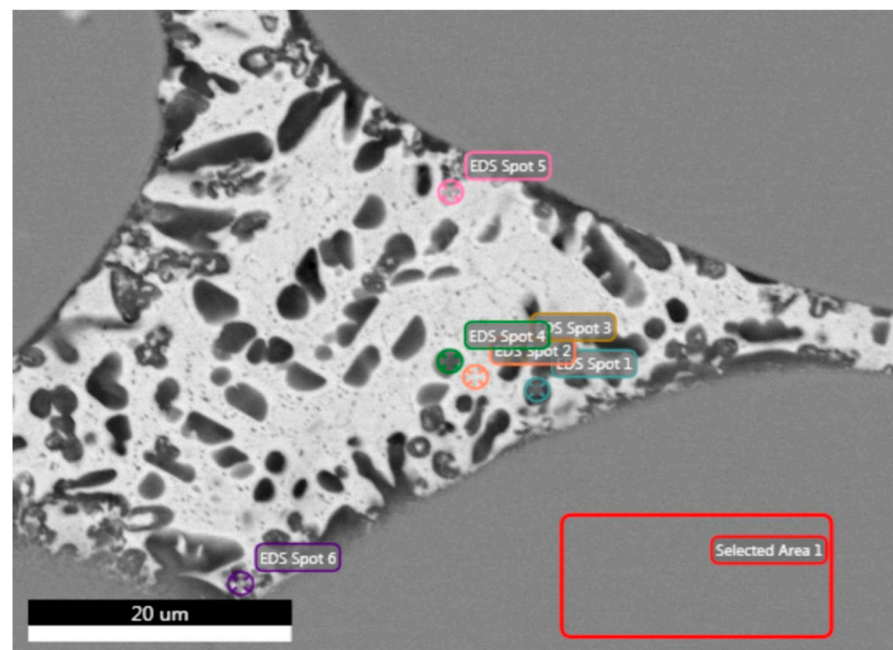


Figure 8. EDS quant maps of as-cast sample A-DD'.



For the heat-treated samples, analysis was conducted for the three samples T16WQ, T16AC and T16FC. FESEM analysis for T16WQ took place, as shown in Figure 9. Results of Area 1 showed that  $\alpha'$  is a Cu–Zn–Al phase and  $\beta'$  is a Sn phase (Table 8 and Figure 10). Analysis of samples T16AC (Figures 11 and 12) and T16FC (Figures 13 and 14) showed that phases  $\alpha'$  and  $\beta'$  exhibit the same composition in all heat-treated samples studied (Tables 9 and 10). Phase  $\gamma'$ , which does not form in water-quenched samples, is a Zn-rich Zn–Cu–Al phase. The particles that appeared in water-quenched and air-cooled samples in the volume of phase  $\beta$  showed a significant oxygen content (Spots 1, 3, 4, 5, 6 in Figure 9 & Spots 2, 4, 6, in Figure 11). Quant maps show the distribution of alloying elements (Figures 10, 12 and 14). Note that the dark feature in Figure 12 is indicated by the EDS map to be a relatively large oxide. As casting was performed by VIM, these oxides likely result from the heat treatments in air, which was carried out to replicate typical industrial processes. Such oxides may have an impact on properties, affecting the hardness and brittleness for example. As the oxides form within the Sn phase, reduction of the amount of Sn in the alloy in further compositional refinement may help to reduce or remove any negative effect they have on these properties.



**Figure 9.** FESEM backscatter electron microstructure with EDS on selected phases for sample T16WQ.

**Table 8.** Elemental composition of the manufactured alloy in sample T16WQ obtained by EDS.

Analysis/ Elements	Spot 1 (at. %)	Spot 2 (at. %)	Spot 3 (at. %)	Spot 4 (at. %)	Spot 5 (at. %)	Spot 6 (at. %)	Area 1 (at. %)
O	15.13	0.00	14.71	19.35	11.40	7.76	2.31
Cu	14.18	4.20	5.99	5.59	3.49	24.32	54.66
Al	9.75	1.80	5.46	3.94	10.11	20.56	20.08
Zn	39.62	10.69	25.58	9.33	11.69	13.80	22.79
Sn	21.32	83.32	48.27	61.79	63.30	33.55	0.16

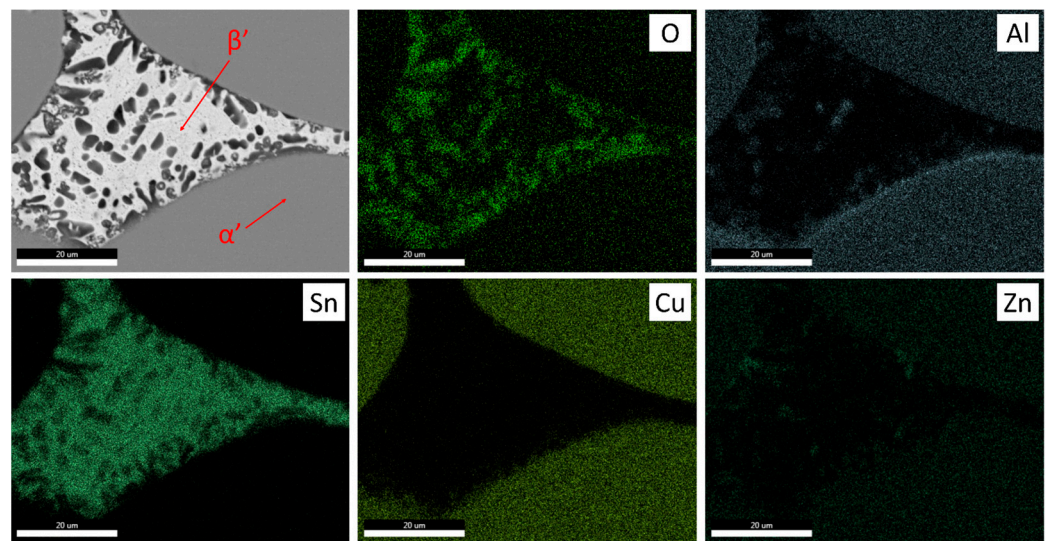


Figure 10. EDS quant maps of sample T16WQ.

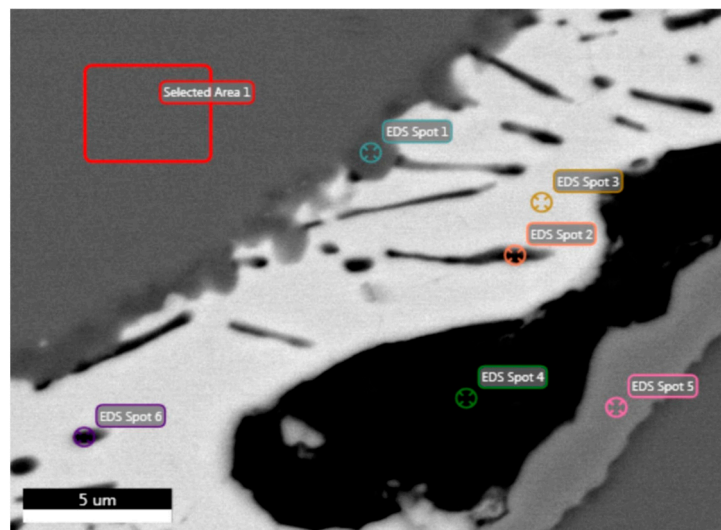


Figure 11. FESEM backscatter electron microstructure with EDS on selected phases for sample T16AC.

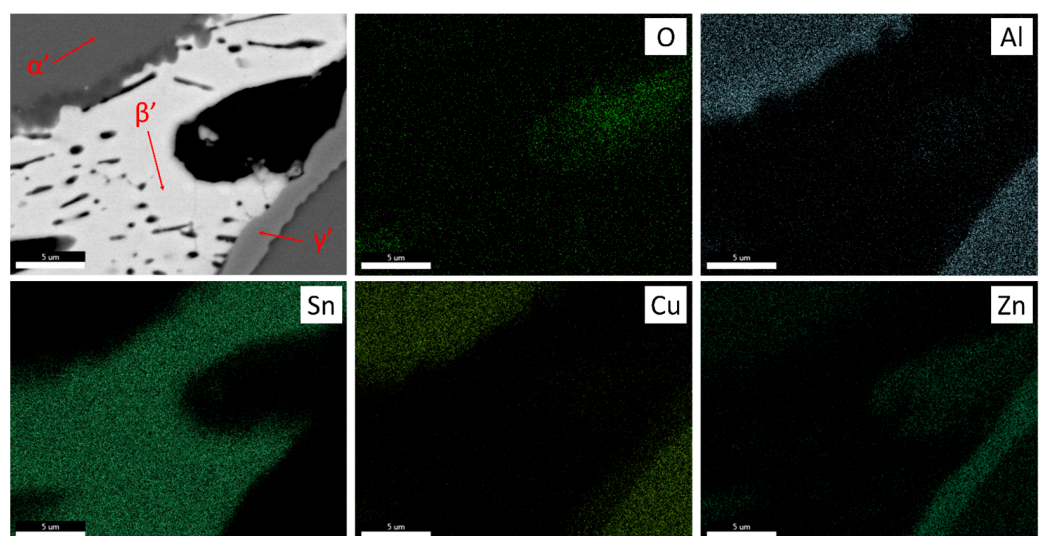


Figure 12. EDS quant maps of sample T16AC.



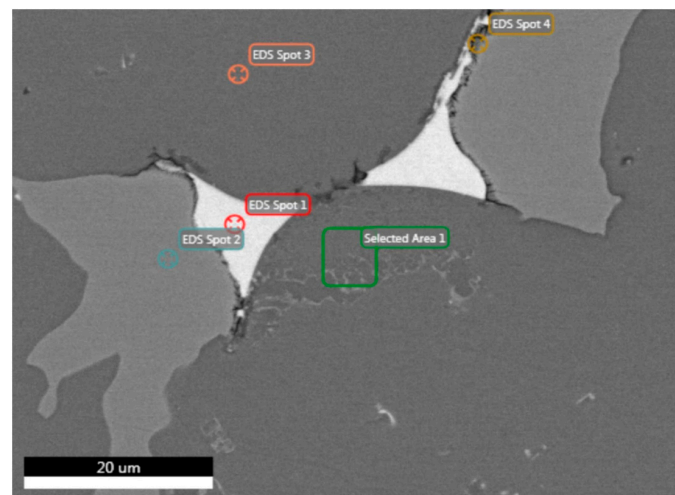


Figure 13. FESEM backscatter electron microstructure with EDS on selected phases for sample T16FC.

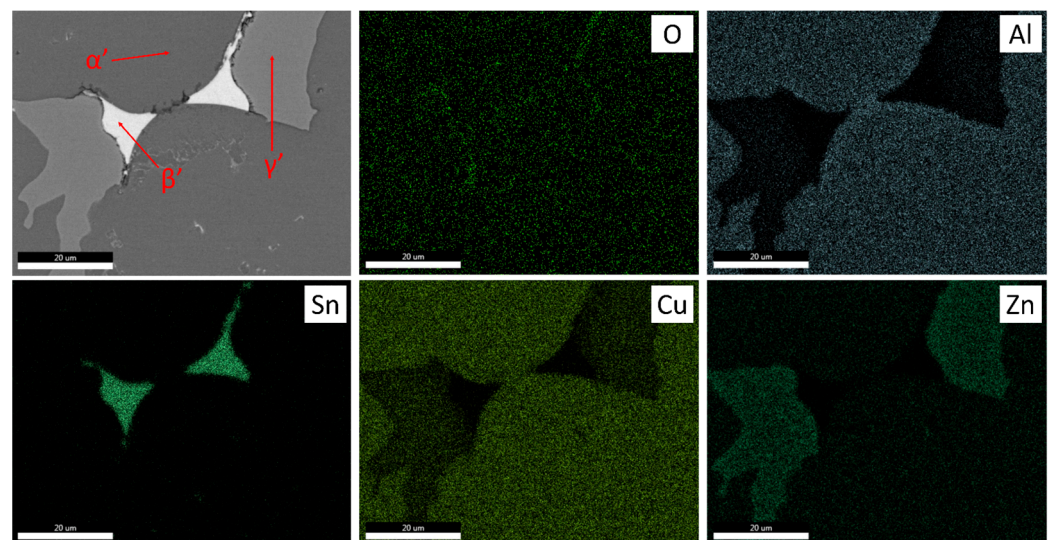


Figure 14. EDS quant maps of sample T16FC.

Table 9. Elemental composition of the manufactured alloy in sample T16AC obtained by EDS.

Analysis/ Elements	Spot 1 (at. %)	Spot 2 (at. %)	Spot 3 (at. %)	Spot 4 (at. %)	Spot 5 (at. %)	Spot 6 (at. %)	Area 1 (at. %)
O	3.40	7.22	3.29	11.70	1.08	3.54	1.59
Cu	10.71	10.27	3.08	10.88	23.24	1.88	53.75
Al	10.65	1.39	0.31	4.96	3.49	0.56	19.54
Zn	8.95	53.20	5.02	52.97	71.78	4.85	24.75
Sn	66.29	27.92	88.31	19.49	0.40	89.16	0.36

Table 10. Elemental composition of the manufactured alloy in sample T16FC obtained by EDS.

Analysis/ Elements	Spot 1 (at. %)	Spot 2 (at. %)	Spot 3 (at. %)	Spot 4 (at. %)	Area 1 (at. %)
O	0.00	0.00	0.00	2.64	0.24
Cu	5.98	35.76	61.28	26.46	54.92
Al	0.22	0.90	11.75	0.76	21.59
Zn	4.94	63.17	26.46	69.42	22.98
Sn	88.85	0.17	0.52	0.73	0.26



From the analysis above, it is concluded that the phases formed in the as-cast state,  $\alpha$ ,  $\beta$  and  $\gamma$ , are the same phases as  $\alpha'$ ,  $\beta'$  and  $\gamma'$  in the heat-treated samples. Table 11 summarizes the three phases and their chemical composition as measured by EDS analysis in the four studied samples. The mean values of phases  $\beta$  and  $\gamma$  exhibit important deviations due to the interference of phase  $\alpha$ . Nevertheless, the absence of  $\gamma$  in the WQ condition indicates that adequate control of the Sn content could lead to the development of a dual-phase microstructure consisting of a Cu–Zn–Al matrix phase alongside finer Sn islands. This is therefore a microstructure directly comparable to that typically encountered in conventional brasses. Furthermore, the chemical composition of the  $\alpha$  phase potentially corresponds to a beta-brass (BCC), which aligns with the CALPHAD predictions but contradicts pyMPEA.

**Table 11.** Phases composition of the manufactured alloy in samples A2-DD', T16WQ, T16AC and T16FC obtained by EDS.

Elements/ Phases	$\alpha$ (at. %)	$\beta$ (at. %)	$\gamma$ (at. %)
Cu	$54.3 \pm 0.6$	$5.6 \pm 2.7$	$27.9 \pm 6.9$
Al	$20.5 \pm 0.9$	$0.9 \pm 0.8$	$2.3 \pm 1.3$
Zn	$23.7 \pm 0.9$	$7.0 \pm 2.7$	$69.1 \pm 5.1$
Sn	$0.3 \pm 0.1$	$85.4 \pm 3.8$	$0.3 \pm 0.1$

Summarizing, in Figure 15, the effect of the heat-treatment scheme on the phase transformation is depicted in a schematic diagram, where the typical microstructure of the alloy at each condition is presented.

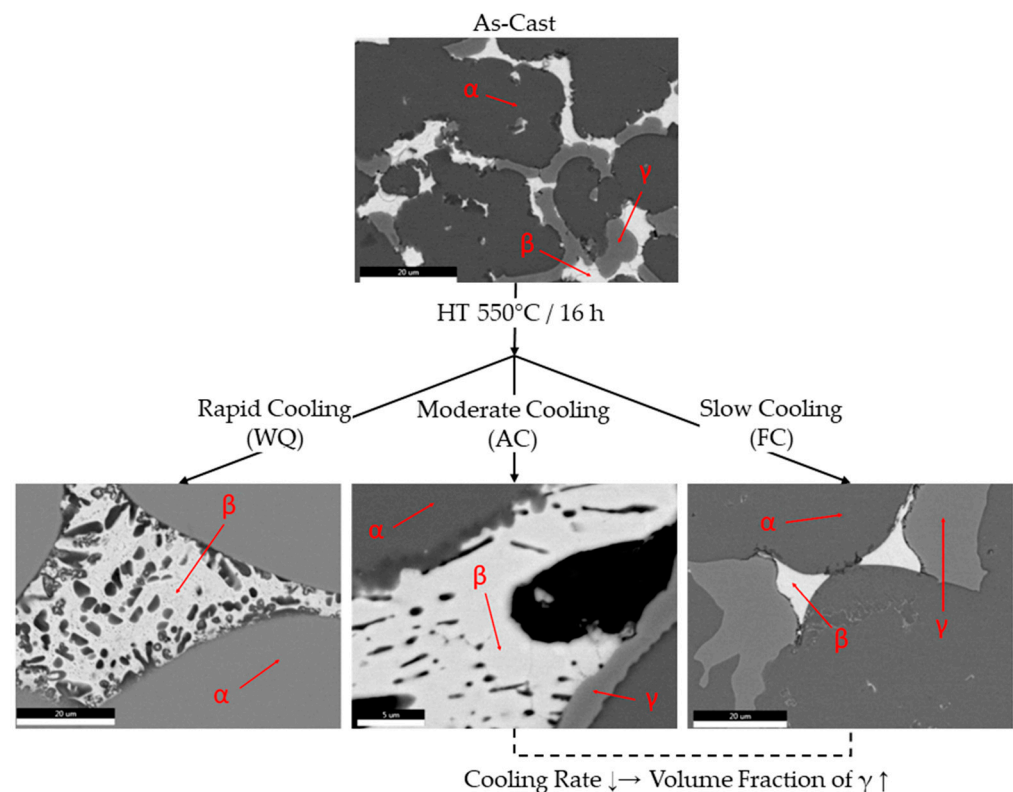


**Figure 15.** Phase transformation according to heat treatments.

### 3.5. Mechanical and Physical Properties

In order to investigate and evaluate the mechanical properties of the as-cast and heat-treated alloys, hardness tests were conducted at room temperature, as shown in Figures 16 and 17. The microhardness tests performed on the as-cast samples showed that

the average hardness of the cast alloys A and B was approximately 377 and 378 HV<sub>0.2</sub>, respectively. The values of the hardness measurements in each sample showed significant deviation, as is seen from observations during the hardness test conduction and the elevated values of the standard deviation in the dataset. This, and the difference of the hardnesses of the alloys in general, is due to the different properties of the phases, and the microstructures in which they are arranged (with variation in how the indent interacts with these microstructures). The parent phase CuZnAl is a quite hard phase, with a measured hardness around 450 HV<sub>0.2</sub>. The other two phases are the Sn-rich phase, which is a very soft phase with a hardness approximating around 25–30 HV<sub>0.2</sub>, and the Zn<sub>x</sub>Cu<sub>y</sub> ( $x = 65\text{--}70$  at. %,  $y = 30\text{--}35$  at. %) phase, which is the hardest phase, with a hardness around 600 HV<sub>0.2</sub>. The response of the Zn<sub>x</sub>Cu<sub>y</sub> phase to indentation is similar to the hard  $\gamma$ -phase of conventional brasses.

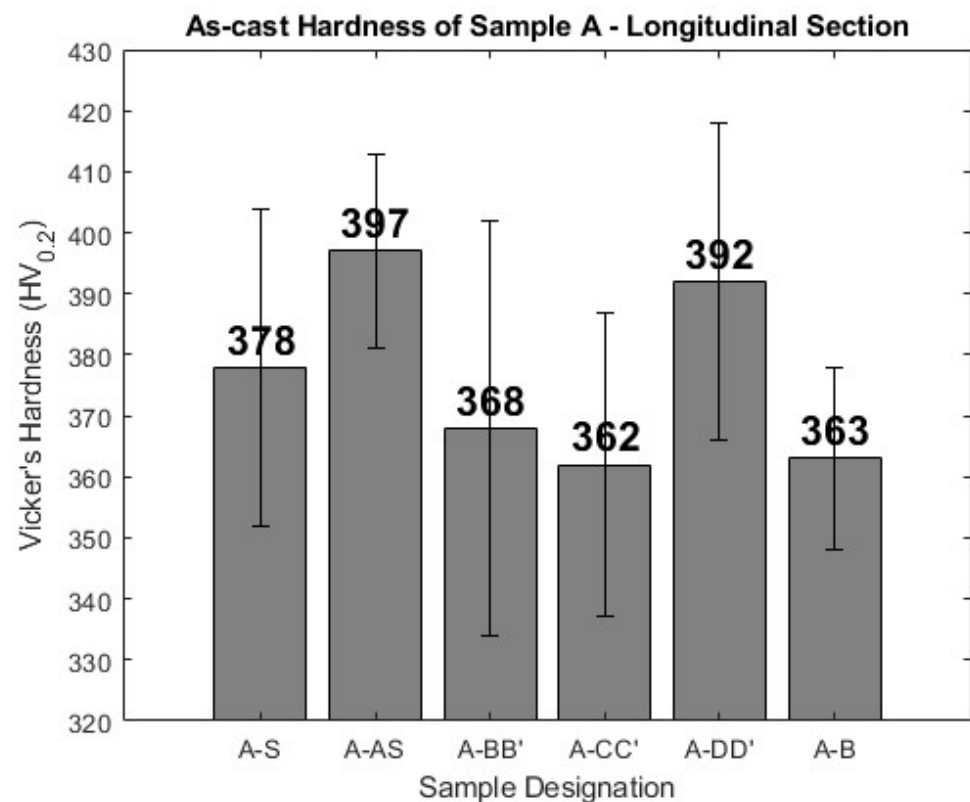


**Figure 16.** Comparison of hardness values in as-cast specimens sectioned from sample A.

It is evident from Figure 18 that the designed alloy's ratio of hardness to density is highly enhanced compared with five commonly used brasses and Cu-based alloys. While good mechanical performance encompasses a much wider range of characteristics than can be assessed by indentation alone, hardness is a particularly suitable measure for some properties, such as abrasion and wear resistance. This novel material combines reduced density and increased hardness and could offer an alternative for applications where conventional Cu-alloys and brass or bronze alloys have limitations.

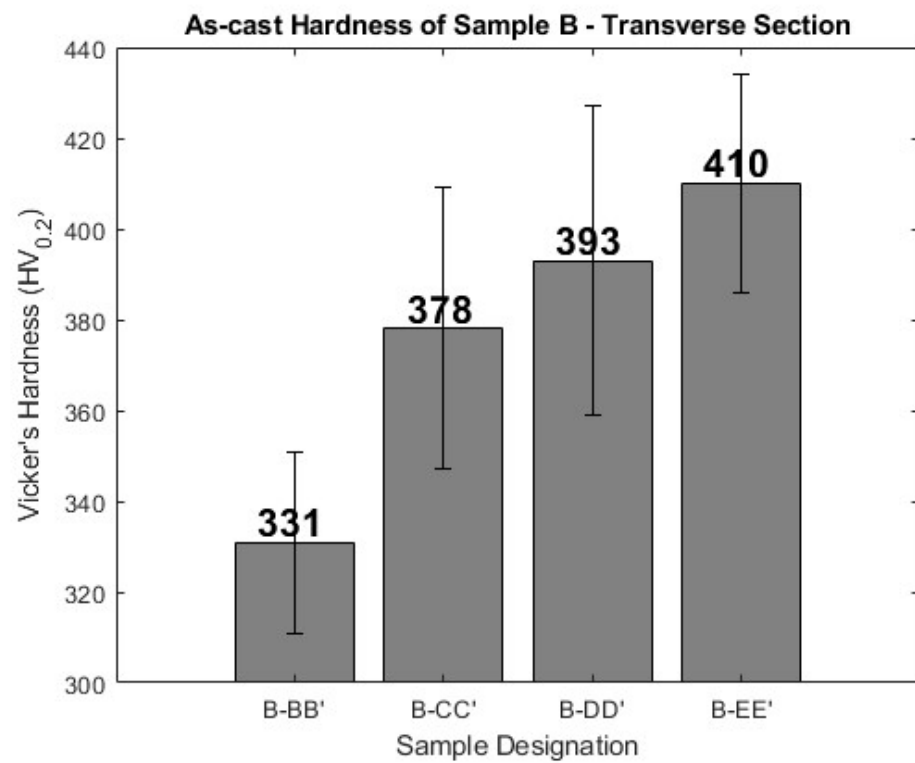


Figure 17. Comparison of hardness values in as-cast specimens sectioned from sample B.

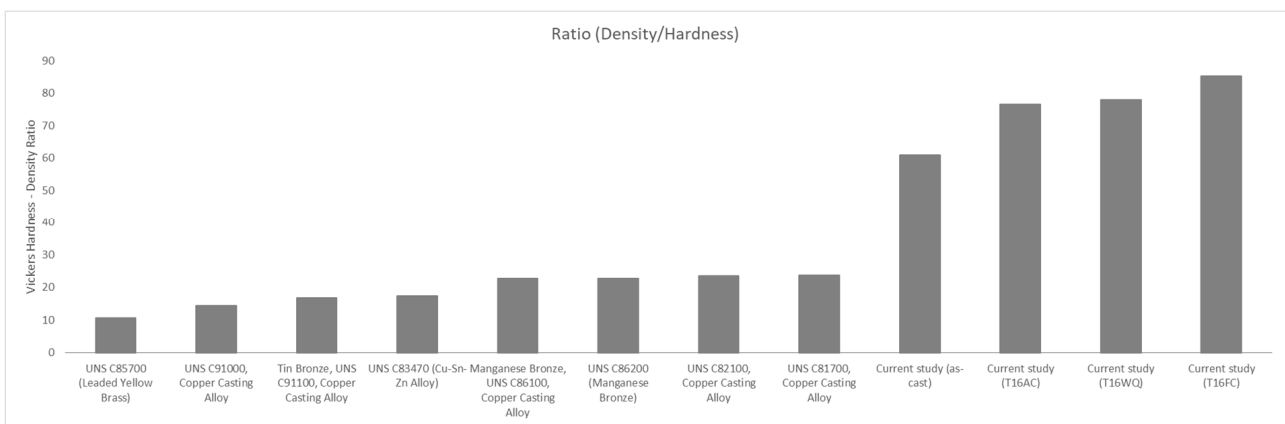


Figure 18. Comparative diagram of strength (as gauged by the hardness) and density ratio for current study and various Cu-based alloys in literature.

The mean hardness of the heat-treated samples was estimated at 499 HV<sub>0.2</sub>, regardless of the cooling path followed. As shown in Figure 19, the hardness values between samples subjected to different cooling rates showed significant deviations. Specifically, the furnace-cooled samples seem to show a slightly higher hardness value compared with the other heat-treated samples, which is possibly attributed to the formation of phase  $\gamma$  or the increase in the volume fraction of phase  $\alpha$ .

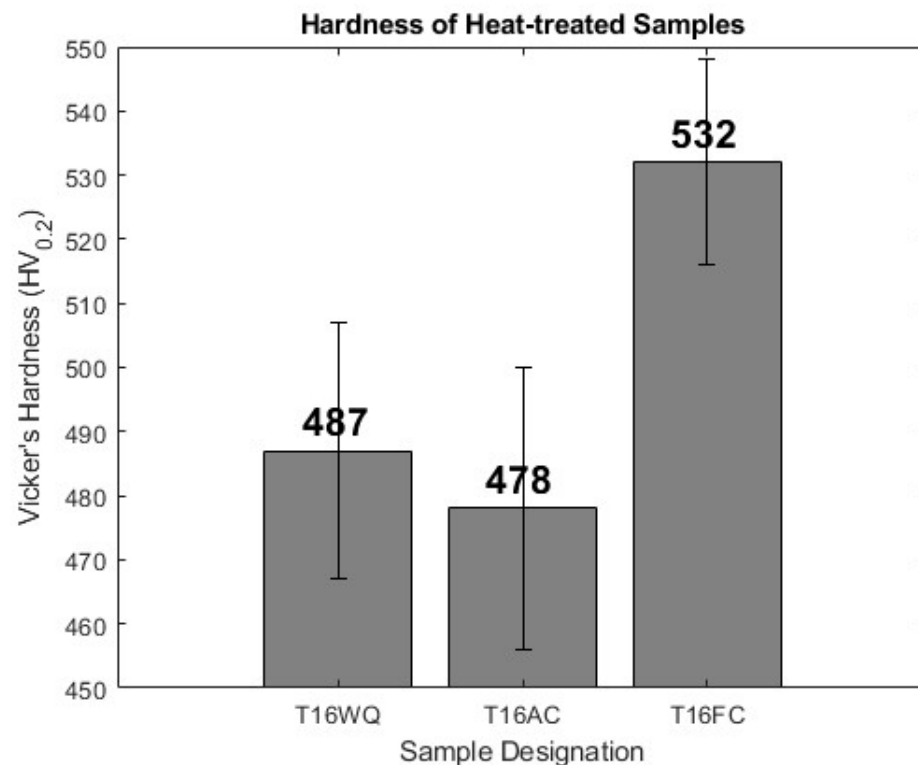


Figure 19. Comparison of hardness values for heat-treated samples.

#### 4. Conclusions

In this work, a novel lead-free MEB ( $\text{Cu}_{50}\text{Al}_{20}\text{Zn}_{25}\text{Sn}_5$  at. %) was successfully developed, with a density of  $6.86 \text{ gr/cm}^3$  and manufactured via VIM, aided by pyMPEA and CALPHAD predictions. It should be underlined that this is a larger scale cast, allowing for the observation of macrosegregation phenomena in multicomponent alloys. The alloy was then subjected to various heat treatments at  $550 \text{ }^\circ\text{C}$  of different durations and cooling rates and was evaluated in terms of its microstructural constituents and hardness. Both pyMPEA and CALPHAD indicated an increased likelihood of formation of a stable matrix phase accompanied by a range of IMs and insoluble elemental Sn particles, which was verified experimentally. It was also discovered that in the heat-treated condition post water quenching the alloy would only consist of a matrix phase accompanied by coarse Sn islands. Additionally, the alloy possessed significantly greater hardness compared with conventional brasses. Therefore, it would be possible to attain a microstructure reminiscent of that encountered in conventional brasses by reducing the amount of Sn, thus forming finer islands. As such, the MEB developed within this work presents a potential candidate for further development and utilization within novel Pb-free brass grades. The main findings are summarized below:

- The high cooling rate of the casting process led to the absence of a columnar solidification zone in the cast material.
- The ingot was characterized by notable macrosegregation phenomena, with the Al and Sn content complementing each other, moving from the top to the bottom of the ingot.
- Three phases were observed in the as-cast and heat-treated samples: the primary phase  $\text{Cu}_{55}\text{Zn}_{25}\text{Al}_{20}$ , pure Sn particles and the IM phase  $\text{Zn}_x\text{Cu}_y$  ( $x = 65\text{--}70$  at. %,  $y = 30\text{--}35$  at. %). Phase  $\gamma$  is likely to form during exposure at lower temperatures as it was not observed after rapid cooling, while its volume fraction was reduced in the air-cooled sample compared with the furnace-cooled one.
- The primary phase showed notable thermodynamic stability, remaining unaffected throughout all heat-treatment schemes and can be used as a basis for future alloy design.

- The IM phase and Sn particles were significantly affected by the cooling rate, where, in water-quenched and air-cooled samples, dark small-size particles appeared within the volume of the elemental Sn islands. The shape of these particles was also affected by the cooling rate. The average specific hardness of the material was higher than that of most conventional brass and bronze alloys. The hardness was strongly dependent on the heat treatments, attaining its maximum value in the FC condition.

**Author Contributions:** Conceptualization, S.C., P.S. and S.P. (Sofia Papadopoulou); Methodology, S.C., P.S. and S.P. (Sofia Papadopoulou); Software, S.C. and P.S.; Validation, S.C., S.M. and P.S.; Formal Analysis, S.C., S.M. and P.S.; Investigation, S.C., S.M. and P.S.; Resources, R.G.; Writing—Original Draft Preparation, S.C. and S.M.; Writing—Review and Editing, S.C., S.M., P.S. and S.P. (Sofia Papadopoulou); Visualization, S.C. and P.S.; Supervision, S.C., P.S. and S.P. (Spyros Papaefthymiou); Project Administration, R.G. and S.P. (Spyros Papaefthymiou). All authors have read and agreed to the published version of the manuscript.

**Funding:** P.S. and R.G. would like to acknowledge funding from EPSRC grant (EP/L016273), the Centre for Doctoral Training in Advanced Metallic Systems. The other authors received no external funding.

**Data Availability Statement:** The raw data supporting the conclusions of this article will be made available by the authors on request.

**Acknowledgments:** The authors express their gratitude to the Hellenic Research Centre for Metals-ELKEME S.A. and University of Sheffield for supporting this research. We thank Y. Azakli from the University of Sheffield for the design and realization of the casting trials.

**Conflicts of Interest:** The authors declare no conflicts of interest.

## References

1. Panagopoulos, C.N.; Georgiou, E.P.; Simeonidis, K. Lubricated Wear Behavior of Lead- $\alpha$  Brass. *Tribol. Int.* **2012**, *50*, 1–5. [[CrossRef](#)]
2. Achiței, D.C.; Minciună, M.G.; Vizureanu, P.; Sandu, A.V.; Cimpoesu, R.; Istrate, B. Study on Structure and Properties of CuZn40Pb Alloy. *IOP Conf. Ser. Mater. Sci. Eng.* **2016**, *133*, 012015. [[CrossRef](#)]
3. Kuyucak, S.; Sahoo, M. A Review of the Machinability of Copper-Base Alloys. *Can. Metall. Q.* **1996**, *35*, 1–15. [[CrossRef](#)]
4. Johansson, J.; Persson, H.; Ståhl, J.-E.; Zhou, J.-M.; Bushlya, V.; Schultheiss, F. Machinability Evaluation of Low-Lead Brass Alloys. *Procedia Manuf.* **2019**, *38*, 1723–1730. [[CrossRef](#)]
5. Hrechuk, A.; Bushlya, V.; M'Saoubi, R.; Ståhl, J.-E. Quantitative Analysis of Chip Segmentation in Machining Using an Automated Image Processing Method. *Procedia CIRP* **2019**, *82*, 314–319. [[CrossRef](#)]
6. Stavroulakis, P.; Toulfatzis, A.I.; Pantazopoulos, G.A.; Paipetis, A.S. Machinable Lead- and Eco-Friendly Brass Alloys for High Performance Manufacturing Processes: A Critical Review. *Metals* **2022**, *12*, 246. [[CrossRef](#)]
7. Momeni, A.; Ebrahimi, G.R.; Faridi, H.R. Effect of Chemical Composition and Processing Variables on the Hot Flow Behavior of Lead-Brass Alloys. *Mater. Sci. Eng. A* **2015**, *626*, 1–8. [[CrossRef](#)]
8. Kozana, J.; Garbacz-Klempka, A.; Piękoś, M. Lead-Free Casting Brasses. Investigations of the Corrosion Resistance and Shaping of Microstructure and Properties. *Arch. Foundry Eng.* **2019**, *2*, 113–118. [[CrossRef](#)]
9. Nobel, C.; Hofmann, U.; Klocke, F.; Veselovac, D.; Puls, H. Application of a New, Severe-Condition Friction Test Method to Understand the Machining Characteristics of Cu–Zn Alloys Using Coated Cutting Tools. *Wear* **2015**, *344–345*, 58–68. [[CrossRef](#)]
10. Adineh, M.; Doostmohammadi, H.; Raiszadeh, R. Effect of Si and Al on the Microstructure, Mechanical Properties and Machinability of 65Cu-35Zn Brass. *Iran. J. Mater. Sci. Eng.* **2019**, *16*, 21–32.
11. Rajabi, Z.; Doostmohammadi, H. Effect of Addition of Tin on the Microstructure and Machinability of  $\alpha$ -Brass. *Mater. Sci. Technol.* **2018**, *34*, 1218–1227. [[CrossRef](#)]
12. Yang, C.; Ding, Z.; Tao, Q.C.; Liang, L.; Ding, Y.F.; Zhang, W.W.; Zhu, Q.L. High-Strength and Free-Cutting Silicon Brasses Designed via the Zinc Equivalent Rule. *Mater. Sci. Eng. A* **2018**, *723*, 296–305. [[CrossRef](#)]
13. Taha, M.A.; El-Mahallawy, N.A.; Hammouda, R.M.; Moussa, T.M.; Gheith, M.H. Machinability Characteristics of Lead Free-Silicon Brass Alloys as Correlated with Microstructure and Mechanical Properties. *Ain Shams Eng. J.* **2012**, *3*, 383–392. [[CrossRef](#)]
14. Han, H.B.; Huang, X.M.; Wu, Y.C.; Qin, Y.Q.; Cao, J.L. Microstructure and Properties of a Bismuth-Brass. *Adv. Mater. Res.* **2012**, *486*, 270–273. [[CrossRef](#)]
15. Zhuo, H.; Tang, J.; Xue, Y.; Ye, N. Preparation of Lead-Free Free-Cutting Graphite Brasses by Graphitization of Cementite. *Trans. Nonferrous Met. Soc. China* **2015**, *25*, 3252–3257. [[CrossRef](#)]
16. Zhang, X.; Ma, C.; Li, S.; Pan, D.; Zheng, F. Interface Design of Lead-Free Free-Cutting Titanium Reinforced Graphite Brass Composites and Its Effect on Mechanical Properties and Cutting Performance. *Mater. Sci. Eng. A* **2020**, *774*, 138909. [[CrossRef](#)]



17. Lee, B.J.; Kim, W.H.; Park, C.M.; Cho, Y.R.; Jeong, M.J. Leadless Free-Cutting Copper Alloy and Method for Producing the Same. U.S. Patent No. 9840758B2, 12 December 2017.
18. Zheng, E.; Ye, D.; Chao, G.; Zhang, B.; Fu, J.; Zhang, C. Free-Cutting Copper Alloy with Excellent Hot Forging Performance and Preparation Method Thereof. CN113106289B, 25 March 2023.
19. Recep, A.; Semih, Ö. Production of a Lead-Free Brass Alloy with the Improved Machinability. TR202018149A2, 23 May 2022.
20. Reetz, B.; Münch, T.; Plett, T. Lead-Free Cu-Zn Alloy. U.S. Patent No. 20220136085A1, 5 May 2022.
21. Toulfatzis, A.; Pantazopoulos, G.; David, C.; Sagris, D.; Paipetis, A. Final Heat Treatment as a Possible Solution for the Improvement of Machinability of Pb-Free Brass Alloys. *Metals* **2018**, *8*, 575. [[CrossRef](#)]
22. Amaral, L.; Quinta, R.; Silva, T.E.; Soares, R.M.; Castellanos, S.D.; De Jesus, A.M. Effect of Lead on the Machinability of Brass Alloys Using Polycrystalline Diamond Cutting Tools. *J. Strain Anal. Eng. Des.* **2018**, *53*, 602–615. [[CrossRef](#)]
23. Cantor, B.; Chang, I.T.H.; Knight, P.; Vincent, A.J.B. Microstructural Development in Equiatomic Multicomponent Alloys. *Mater. Sci. Eng. A* **2004**, *375–377*, 213–218. [[CrossRef](#)]
24. Miracle, D.B.; Senkov, O.N. A Critical Review of High Entropy Alloys and Related Concepts. *Acta Mater.* **2017**, *122*, 448–511. [[CrossRef](#)]
25. Bhadeshia, H.K.D.H. High Entropy Alloys. *Mater. Sci. Technol.* **2015**, *31*, 1139–1141. [[CrossRef](#)]
26. Chaskis, S.; Stachouli, E.; Gavalas, E.; Bouzouni, M.; Papaefthymiou, S. Microstructure, Phase Formation and Heat-Treating of Novel Cast Al-Mg-Zn-Cu-Si Lightweight Complex Concentrated Aluminum Based Alloy. *Materials* **2022**, *15*, 3169. [[CrossRef](#)] [[PubMed](#)]
27. Chaskis, S.; Bouzouni, M.; Gavalas, E.; Loukadakis, V.; Papaefthymiou, S. Development of Complex Concentrated Alloys (CCAs) Utilizing Scrap to Preserve Critical Raw Materials. In Proceedings of the International Conference on Raw Materials and Circular Economy. *Mater. Proc.* **2021**, *5*, 109.
28. Laws, K.J.; Crosby, C.; Sridhar, A.; Conway, P.; Koloadin, L.S.; Zhao, M.; Aron-Dine, S.; Bassman, L.C. High Entropy Brasses and Bronzes—Microstructure, Phase Evolution and Properties. *J. Alloys Compd.* **2015**, *650*, 949–961. [[CrossRef](#)]
29. Nagase, T.; Shibata, A.; Matsumuro, M.; Takemura, M.; Semboshi, S. Alloy Design and Fabrication of Ingots in Cu-Zn-Mn-Ni-Sn High-Entropy and Cu-Zn-Mn-Ni Medium-Entropy Brasses. *Mater. Des.* **2019**, *181*, 107900. [[CrossRef](#)]
30. *Copper Casting Alloys*; Copper Development Association: New York, NY, USA, 1994.
31. Subedi, U.; Kunwar, A.; Coutinho, Y.A.; Gyanwali, K. pyMPEALab Toolkit for Accelerating Phase Design in Multi-Principal Element Alloys. *Met. Mater. Int.* **2022**, *28*, 269–281. [[CrossRef](#)]
32. Smallman, R.E.; Ngan, A.H.W. *Modern Physical Metallurgy*, 8th ed.; Elsevier: Amsterdam, The Netherlands, 2014; ISBN 9780080982045.
33. Zhang, Y.; Zhou, Y.J.; Lin, J.P.; Chen, G.L.; Liaw, P.K. Solid-Solution Phase Formation Rules for Multi-component Alloys. *Adv. Eng. Mater.* **2008**, *10*, 534–538. [[CrossRef](#)]
34. Yang, X.; Zhang, Y. Prediction of High-Entropy Stabilized Solid-Solution in Multi-Component Alloys. *Mater. Chem. Phys.* **2012**, *132*, 233–238. [[CrossRef](#)]
35. Pickering, E.J.; Jones, N.G. High-Entropy Alloys: A Critical Assessment of Their Founding Principles and Future Prospects. *Int. Mater. Rev.* **2016**, *61*, 183–202. [[CrossRef](#)]
36. Andersson, J.-O.; Helander, T.; Höglund, L.; Shi, P.; Sundman, B. Thermo-Calc & DICTRA, Computational Tools for Materials Science. *Calphad* **2002**, *26*, 273–312. [[CrossRef](#)]
37. Ahlers, M. Martensite and Equilibrium Phases in Cu-Zn and Cu-Zn-Al Alloys. *Prog. Mater. Sci.* **1986**, *30*, 135–186. [[CrossRef](#)]
38. Kim, S.-J.; Kim, K.-S.; Kim, S.-S.; Kang, C.-Y.; Sukanuma, K. Characteristics of Zn-Al-Cu Alloys for High Temperature Solder Application. *Mater. Trans.* **2008**, *49*, 1531–1536. [[CrossRef](#)]
39. Alkan, S.; Wu, Y.; Ojha, A.; Sehitoglu, H. Transformation Stress of Shape Memory Alloy CuZnAl: Non-Schmid Behavior. *Acta Mater.* **2018**, *149*, 220–234. [[CrossRef](#)]
40. Paul, C.; Sellamuthu, R. The Effect of Sn Content on the Properties of Surface Refined Cu-Sn Bronze Alloys. *Procedia Eng.* **2014**, *97*, 1341–1347. [[CrossRef](#)]
41. Sanchez, J.M.; Pascual, A.; Vicario, I.; Albizuri, J.; Guraya, T.; Galarraga, H. Microstructure and Phase Formation of Novel Al80Mg5Sn5Zn5X5 Light-Weight Complex Concentrated Aluminum Alloys. *Metals* **2021**, *11*, 1944. [[CrossRef](#)]
42. Balazinski, M.; Songmene, V.; Kishawy, H.A. Analyzing the Machinability of Metal Matrix Composites. In *Machining Technology for Composite Materials*; Elsevier: Amsterdam, The Netherlands, 2012; pp. 394–411, ISBN 9780857090300.
43. Vilarinho, C.; Davim, J.P.; Soares, D.; Castro, F.; Barbosa, J. Influence of the Chemical Composition on the Machinability of Brasses. *J. Mater. Process. Technol.* **2005**, *170*, 441–447. [[CrossRef](#)]
44. Stavroulakis, P.; Freeman, C.L.; Patel, D.; Utton, C.; Goodall, R. Successful Prediction of the Elastic Properties of Multiphase High Entropy Alloys in the AlTiVCr-Si System through a Novel Computational Approach. *Materialia* **2022**, *21*, 101365. [[CrossRef](#)]

**Disclaimer/Publisher’s Note:** The statements, opinions and data contained in all publications are solely those of the individual author(s) and contributor(s) and not of MDPI and/or the editor(s). MDPI and/or the editor(s) disclaim responsibility for any injury to people or property resulting from any ideas, methods, instructions or products referred to in the content.